Inhibited Degradation of Organic–Inorganic Perovskite-Based Quantum Dot Films via Rapid Annealing Temperatures

Pao-Hsun Huang [1], Pin-Jia Lai [2], Wen-Ray Chen [3], Chuan-Hsi Liu [4,*], Po-Wen Sze [5], Shui-Yang Lien [6,7] and Chien-Jung Huang [2,*]

1   School of Ocean Information Engineering, Jimei University, Jimei District, Xiamen 361021, China
2   Department of Applied Physics, National University of Kaohsiung, Kaohsiung University Rd., Kaohsiung 81148, Taiwan
3   Department of Electronic Engineering, National Formosa University, Wenhua Rd., Yunlin 632301, Taiwan
4   Department of Mechatronic Engineering, National Taiwan Normal University, Heping East Rd., Taipei 10610, Taiwan
5   Department of Electrical Engineering, Kao Yuan University, Zhongshan Rd., Kaohsiung 82151, Taiwan
6   Xiamen Key Laboratory of Development and Application for Advanced Semiconductor Coating Technology, School of Opto-Electronic and Communication Engineering, Xiamen University of Technology, Xiamen 361024, China
7   Department of Materials Science and Engineering, Da-Yeh University, Dacun, Changhua 51591, Taiwan
*   Correspondence: liuch@ntnu.edu.tw (C.-H.L.); chien@nuk.edu.tw (C.-J.H.); Tel.: +886-7-5919475 (C.-J.H.); Fax: +886-7-5919357 (C.-J.H.)

Abstract: General hot-plate heating is used to form a crystal structure of films; however, how to achieve a homogeneous and regulated crystal formation will be a crucial challenge in the future. In this study, based on perovskite-series materials, organic methylamine lead trioxide ($MAPbI_3$) films doped with inorganic lead iodide ($CsPbI_3$) quantum dots (QDs) are treated using the rapid thermal annealing (RTA) process in argon gas to break the crystallization barrier. These RTA-treated perovskite quantum dot (PQD) films at various temperatures of 100–160 °C are detected using X-ray diffraction, X-ray spectroscopy, and absorbance measurements to investigate their structural and optical properties as well as their binding states. The experimental results demonstrate that the PQD film annealed at 120 °C has optimized characteristics, revealing better crystallinity and the lowest content of oxygen atoms (31.4%) and C-O-C bonding (20.1%). A too-high RTA temperature, more than 140 °C, causes severe degradation with the existence of PbI_2. A proper RTA process, an alternative to normal heating and annealing, can effectively inhibit the occurrence of degradation and even usefully improve the performance of PQD films.

Keywords: perovskite; annealing; quantum dots; ligand-assisted reprecipitation

1. Introduction

In the past few years, due to their excellent properties, including long diffusion length, long carrier life, adjustable band gap, and high absorption coefficient [1–5], organic–inorganic halide perovskite-based materials have received much attention, and are being further applied to numerous optoelectronic devices [6–8]. One of the most famous optoelectronics is perovskite solar cells (PSCs), first proposed by Akihiro Kojima et al. in 2009, owing to their sharply increasing power conversion efficiency (PCE) from 3.8 to 25.5% in 2022 [9–11]. The advantage of easy fabrication with low cost also makes PSCs more competitive than conventional silicon solar cells [12]. The general preparation of the film consists of spin-coating the configured precursor solution onto the substrate and then achieving a crystalline structure through annealing the substrate at a specific and desired temperature for a period of time. Annealing as a maintenance process in given conditions is not only used to evaporate the organic polar solvent, but also drive the

crystalline transformation of halide perovskite-based materials, which can control the optical, morphological, and structural properties of films. Many annealing methods, such as physical annealing, thermal annealing, photo-annealing, and solvent annealing, have been proposed and developed to shorten the annealing treatment performance and improve crystal quality. However, the presence of a defect state in halide perovskite-based materials usually leads to a shorter lifetime of photoluminescence [13,14] due to the free-charge trapping induced by inner crystallite boundaries. Feng Xian Xie et al. reported that a denser methylammonium lead halide ($CH_3NH_3PbI_3$, MAPbI$_3$) film via one-step coating was determined after thermal annealing for three hours, suppressing defect formation, and then showing an increased current density [15,16]. Nevertheless, annealing for an excessive time causes the decomposition of MAPbI$_3$ and the extra crystallization of lead (II) iodide (PbI_2) as well as crystal fragmentation [17]. In addition, the degradation caused by moisture and oxygen gas becomes a crucial issue as the MA anion is hygroscopic [18]. The oxygen-induced photo-degradation of MAPbI$_3$ results in decreased stability [19–21]. Philippe et al. reported that in the absence of aqueous oxygen, degradation commonly occurred at an ambient temperature of 100 °C [22].

Obviously, the decrease in oxygen atoms in MAPbI$_3$ films contributes to the inhibition of oxygen defect formation and lowers the degradation with the MA anion. In many studies and our previous research [23,24], the temperature-dependent crystallization of films usually comes from the hot plate of physical annealing, where its heat transfer is in a single direction from the substrate to the film. This asymmetrical heating and its surrounding lower-temperature environment, as well as atmospheric gas, can result in a problematic crystalline barrier and further crystallization inhomogeneity, as shown in our previous paper [23,25,26], leading to the uncontrollable growth of the structure. In addition, thermal annealing and rapid thermal annealing (RTA) as alternative heat transfer occur in all directions [27]. During thermal annealing, atoms migrate in the crystal lattice and the number of dislocations decreases via the diffusion induced by differential concentration, leading to a change in ductility and hardness. Typically, annealing is carried out to relieve stress, increase softness, ductility, and toughness, and/or produce a specific microstructure. Any annealing cycle consists of three stages: heating to the desired temperature, holding or soaking at that temperature, and cooling (usually to room temperature). The processing time and annealing temperature, as well as the processing temperature are important parameters that define the thermal annealing cycle. Among the thermal annealing methods, RTA is also an effective approach to simultaneously accelerate the breaking of the crystallization barrier and suppress oxygen defect formation. Compared to annealed- [28] and RTA-treated [29] metal oxide materials, few studies have proposed the RTA-induced crystallization of organic–inorganic halide perovskite-based materials. Meanwhile, after the precursor solution is spun onto the film, this perovskite film starts out in a metastable state with complex internal crystalline phases that can be tuned into intermediate phases using polar solvent via RTA. This result is not only mainly induced by the annealing type, but also influenced by many parameters, such as heat flux, temperature, pressure, time, process gas, raised temperature rate, and cooling type, which are worth investigating in the mechanism of crystallization.

In our past investigation of hot-solvent injection methods [23,25,26], ligand-assisted reprecipitation was mainly used to prepare quantum dots (QDs), due to its advantages such as its simple procedure, lower processing temperature, and flexibility in atmospheric gas. However, most studies still use general hot-plate heating to form a crystal structure. How to achieve a homogeneous and regulated crystal formation will be a crucial challenge in the future. In this paper, to enhance structural stability and optical properties, the concept of achieving cation exchange in an MAPbI$_3$ solution [30–32] is used by doping perovskite-based inorganic quantum dots (QDs) with CsPbI$_3$ synthesized via ligand-assisted reprecipitation preparation [26,33,34]. These innovative perovskite quantum dots (CsPbI$_3$-doped MAPbI$_3$, PQD) films are processed via rapid annealing at different temperatures in the range of 100–160 °C. This RTA process can induce the removal of

solvent to build a supersaturating condition, accelerating perovskite-based nucleation and enhancing the density of the nucleus. To further keep the annealing process from causing more chemical reactions, inert argon gases are used as process gases. The effects of temperature on the optical, structural properties, and oxygen content of PQD films are investigated. The variation in oxygen content with the increasing annealing temperatures is presented. Finally, the inhibition of the oxygen content of PQD films via RTA is demonstrated and discussed.

2. Materials and Methods

2.1. Materials

Table 1 shows all the materials used, which were not further treated. According to our previous investigations [23,25,26], the preparation was carried out in a glove box with moisture and oxygen gas values below 1 ppm.

Table 1. Information about the materials used.

Materials	Value	Units	Note
methylammonium iodide (CH_3NH_3I)	198.75	mg	
cesium iodide (CsI)	20.78	mg	99.9%
lead(II) iodide (PbI_2)	576.25	mg	99.9985%
toluene (C_7H_8)	20	mL	anhydrous 99.8%
hexane			analytical reagent, 97%
oleyl amine ($C_{18}H_{35}NH_2$, OAm)	2.4	mL	90%
dimethyl sulfoxide (($CH_3)_2SO$, DMSO)	0.5	mL	99%
gamma-Butyrolactone ($C_4H_6O_2$, GBL)	0.5	mL	99.9%
dimethylformamide (DMF)	10	mL	

2.2. Synthesis of $CsPbI_3$ QDs and $CH_3NH_3PbI_3$ Solution

As shown in Figure 1, OAm, 0.4 mmol CsI, 0.4 mmol PbI_2, and DMF solvent were mixed and stirred continuously for 10 s to prepare a precursor solution of quantum dots. Then, 1 mL of the precursor solution of quantum dots was added to stirring toluene for 10 s to obtain a crude solution, which was centrifuged at 11,000 rpm for 15 min at an ambient 10 °C. The precipitate was collected and then dispersed in hexane, and the above centrifugation process was repeated twice.
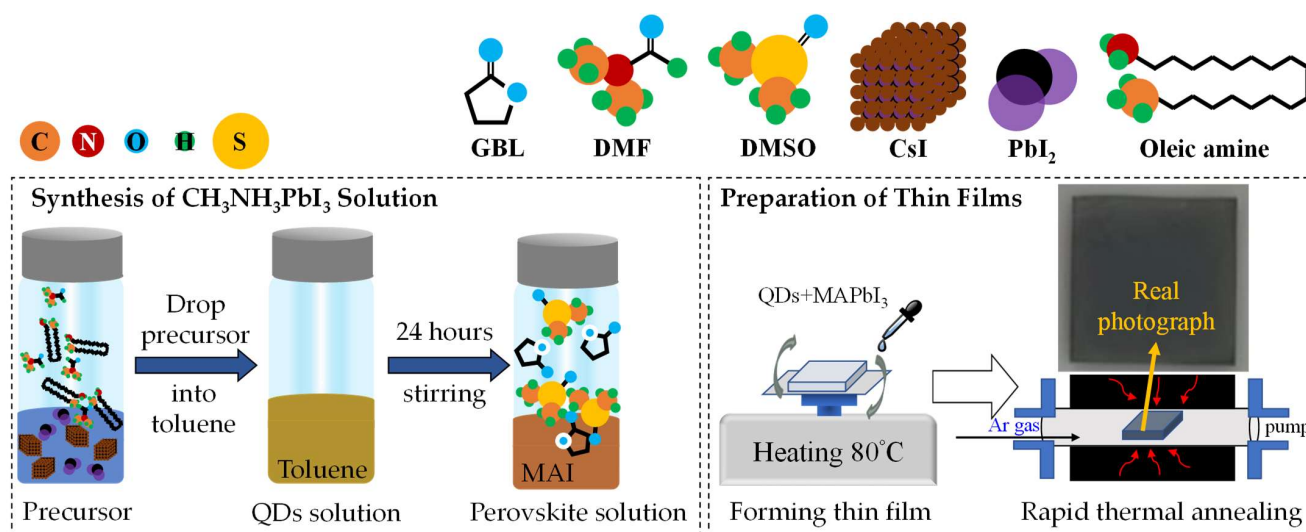

Figure 1. The schematic diagram for the synthesis of $CH_3NH_3PbI_3$ solution and the preparation of thin films, where the real photograph of sample takes place.

Both DMSO and GBL solvents were mixed and then added to the powder mixture of CH_3NH_3I and PbI_2 to form the organic halide perovskite-based solution of $CH_3NH_3PbI_3$. This solution was stirred for one day at 300 rpm in a nitrogen-filled glove box.

2.3. Preparation of Thin Films

The glass substrates were cleaned in an ultra-sonicated system with the deionized water, acetone, and isopropyl alcohol, each for 5 min. The substrate was dried with nitrogen (N_2) gas before surface treatment with oxygen plasma for 2 min.

The PQD films were prepared by spin-coating the mixed solutions of 1 mL $CsPbI_3$ QDs and 1 mL $CH_3NH_3PbI_3$ in a nitrogen-filled glove box. First, 50 μL of the mixed solution was dropped onto the glass substrate, and then was spin-coated in two-steps, with a setting of 1000 rpm for 10 s and then 5000 rpm for 20 s, to ensure the uniform coverage of solution and the film thickness, respectively. Toluene as an anti-solvent method was dropped during spinning in the second step, after 15 s. Thereafter, the film formation was heated using a hot plate in a N_2 environment at 80 °C for 15 min.

2.4. Rapid Thermal Annealing (RTA) Process

The RTA treatment was performed at different temperatures, from 100 to 160 °C. The process time and atmospheric gas of the RTA were 10 min and argon gas (Ar, 99.95%), respectively. The temperature-raised mode and annealing time were set at 10 min. The cooling mode was set to room temperature.

2.5. Characteristic Measurements

The optical properties of the films was detected using the ultraviolet/visible (UV/vis) spectroscopy (HITACHI, U-3900, Tokyo, Japan) to obtain the absorption spectrum. To gain the structural properties, the crystallite phases were measured using grazing incidence X-ray diffraction (XRD), and the data were recorded using a Bruker D8 Discover X-ray diffractometer (Bruker AXS Gmbh, Karlsruhe, Germany) The crystalline phases were characterized at a fixed operating voltage of 40 kV and a fixed current of 40 mA. To perform the chemical states and elemental composition of the films, X-ray photoelectron spectroscopy (XPS, ULVAC-PHI 5000, Kanagawa Prefecture, Japan) was used with a VersaProbe/Scanning ESCA Microprobe, equipping the microfocused Al Kα X-rays (26.4 W, 100 μm), and the analyzer scanned with an area of 500×500 μm^2. The take-off angle of the photoelectron was fixed at 45°. Peak fitting imitating software (Origin85) was used to distinguish the XPS peaks. All measurement procedures were carried out in a dark atmospheric environment.

3. Results

Figure 2a shows the absorbance spectra of $MAPbI_3$ and PQD films in the wavelength range of 350–850 nm. A typical absorption peak at 750 nm is observed. The absorption of $MAPbI_3$ from 350 to 750 nm was enhanced after doping with $CsPbI_3$ QDs. The reason is due to the improved surface structure caused by the cation exchange [35]. Figure 2b also demonstrates the absorbance spectra of PQD films treated with RTA at different temperatures from 100 to 160 °C. It is found that in the wavelength of 600–850 nm, the unchanged absorbance of samples shows that the RTA process effectively enhanced the film quality. Compared to many investigations and our previous studies, this result suggests that the degradation of PbI_2 can be effectively managed using the RTA process. With the increase in temperatures, the PQD films annealed at 120 °C, reaching a maximum performance in the UV region of 350–500 nm due to the matched lattice arrangement induced by small strain [36,37]. An obvious decrease in the absorbance of PQD films was observed at 140–160 °C, which results from the degradation on the film surface, with visible yellow spots which is similar to previous reports [38,39]. A too-high RTA temperature of more than 140 °C causes the decomposition of films and even surface breaking.
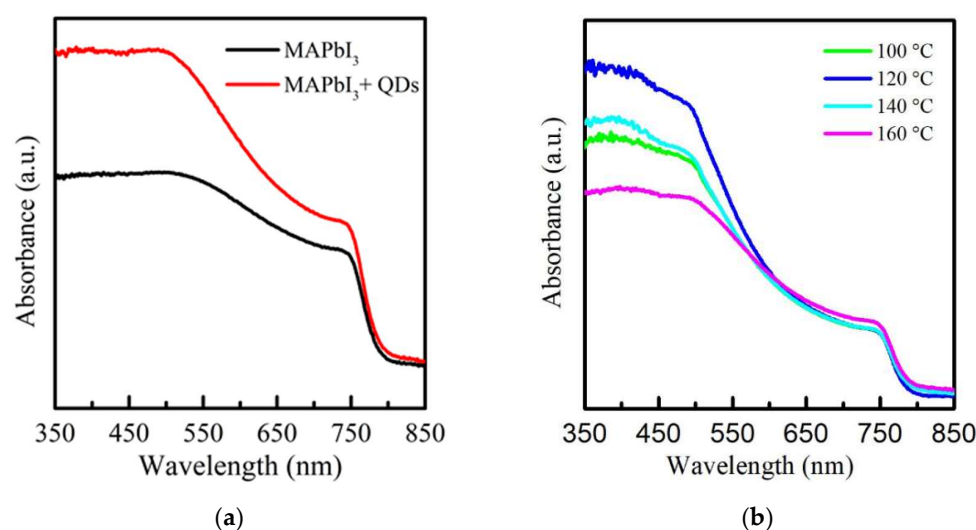
Figure 2. Absorbance spectrum of (**a**) MAPbI$_3$ film without and with doped CsPbI$_3$ QDs and (**b**) the RTA-treated PQD films at the various temperatures from 100 to 160 °C.

In Figure 3, the MAPbI$_3$ and PQD films were analyzed using XRD at different annealing temperatures (100–160 °C). The main peaks of (110) and (220) are observed at 14° and 28° of 2θ, respectively [40,41]. A few minor peaks at (001) and (003) are observed at 12.7° and 38.7°, respectively [42,43], which are usually identified as a PbI$_2$ phase caused by the degradation of MAPbI$_3$ films. Some slight peaks at (113), (112), and (PbI$_2$) in the range of 20°–25° are determined as the intermediate phase during the crystallization process [39]. The decreased intensity of the main (110) peak of the MAPbI$_3$ films induced by CsPbI$_3$ QDs is owing to the existence of a residual ligand (oleylamine) after doping [44], leading to a decrease in the crystallinity of the films. This residual ligand can be effectively removed via the RTA process, revealing the enhancement of the intensity of the (110) peak of the RTA-treated PQD films at 100 and 120 °C. The decreased intensity of the (220) peak at 100 °C may possibly be due to the insufficient cation exchange with the lack of thermal energy. Therefore, the temperature of 120 °C inhibits PbI$_2$ formation, corresponding to the weakened intensity of the (001) peak and resulting in the significant enhancement of the (220) peak of the MAPbI$_3$ films and the better crystallinity of PQD films. However, the temperatures of 140 °C cause the sharply increased intensity of the (001) peak of PbI$_2$. The reason is attributed to the decomposition of MAPbI$_3$ and CsPbI$_3$ QD films. It is found that the degradation of the PQD film annealed by the high temperature in an atmospheric environment demonstrates PbI$_2$ formation, which is consistent with the above description. However, the existence of an oxygen atom is another reason to cause the degradation of PQD films.

The chemical features and element compositions of RTA-treated PQD films at different temperatures of 100–160 °C were investigated using XPS measurement. Figure 4 illustrates the spectra of the O 1s core level in the range of 528–536 eV to research the oxidation of PQD films induced by their hygroscopic nature. It is obviously found that a peak of the MAPbI$_3$ film at 532.04 eV shifts to that of the higher binding energy of PQD films at 532.5 eV. This shift of ~0.5 eV may be due to the residual ligands caused by crystalline defects in turn bonding to oxygen atoms. It is clearly observed that with the increasing RTA temperatures from 100 to 140 °C, there is a decrease in the shift to a lower binding energy at 531.9 eV due to octahedral tilting after doping with cations, further stabilizing the structure and promoting thermal stability [45]. A shift to a higher binding energy at 160 °C is owing to the degradation of the surface of the PQD films, leading to the existence of the PbI$_2$ phase, which is in agreement with the XRD results.
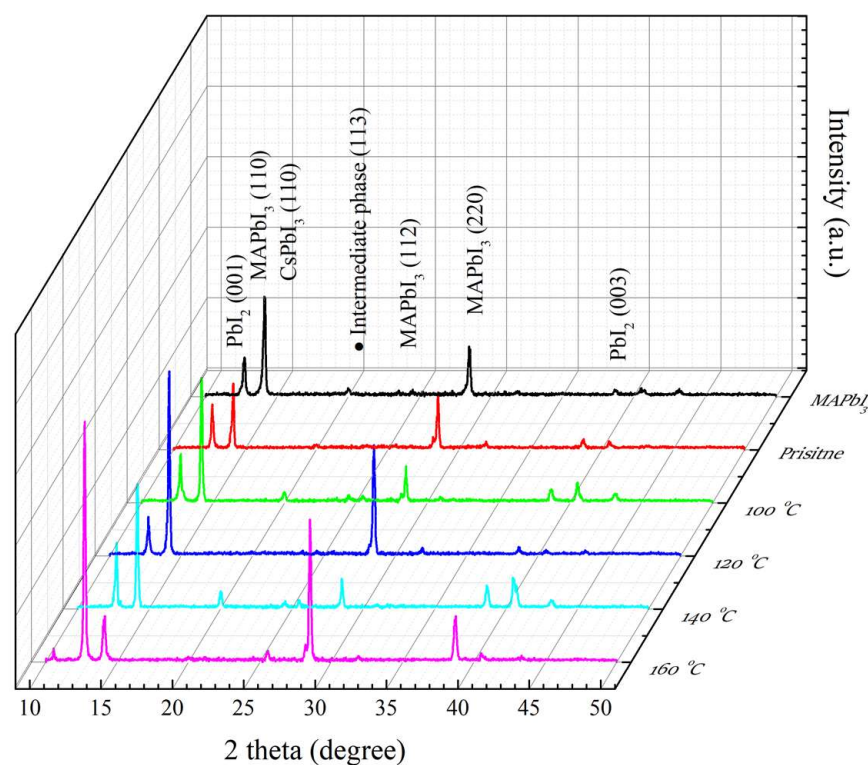
Figure 3. XRD patterns of MAPbI$_3$, and RTA-treated PQD films at different annealing temperatures from 100 to 160 °C.
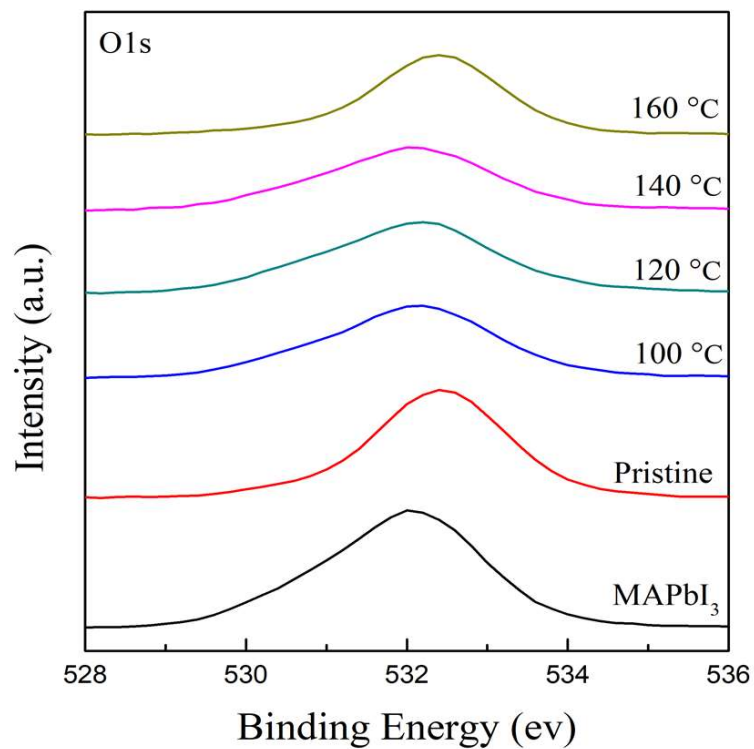

Figure 4. The XPS spectra of O 1s core level for the MAPbI$_3$ and PQD films at different RTA temperatures in the range of 100–160 °C.

The contents of oxygen atom (at%) of all samples are also shown in Table 2. The content of oxygen atoms after doping the CsPbI$_3$ QDs into MAPbI$_3$ exhibits the value from

the highest at 64.3% to 42.8%. This highest value in MAPbI$_3$ films is due to the degradation induced by the light, temperature of the environment, and especially moisture, as well as oxygen. However, the oxygen content of PQD film annealed at 120 °C displays the lowest value of 31.4% and it gradually increases to 33.1 at 140 °C and 40.2% at 160 °C. Thus, the severe degradation of PbI$_2$ is induced by the RTA process at higher temperatures than 140 °C. However, the ratio of carbon to oxygen (C/O) of PQD films demonstrates carbon-containing bonding or substances, suggesting that the peak area of O 1s at different temperatures demonstrates that there may be bonds of oxygen and carbon in the surface of PQD films.

Table 2. The contents of oxygen atoms (at%) of all samples.

Samples	MAPbI$_3$ Films	PQD Films	RTA-Treated PQD Films at Different Temperatures			
			100 °C	120 °C	140 °C	160 °C
Oxygen Content (at%)	64.3	42.8	36.8	31.4	33.1	40.2

Therefore, in order to understand the binding state of the oxygen and carbon atoms in films, in Figure 5, the spectra of the C 1s core level of PQD films at different annealing temperatures were detected (see Figure 5c,f). It is observed that these peaks are located at ~284 eV, despite there being an asymmetric shape observed near higher binding energies. Thus, the peaks of C 1s are further deconvoluted into two major peaks, which are assigned to 284.4 and 285.4 eV. These two peaks are typically presented as the bonding of C-C and C-O-C, respectively [46,47], which is caused by the resulting oxidation of PQD films in the atmospheric environment. The peak areas of the C-C and C-O-C bonding are calculated in Table 3. It is observed that the doping with CsPbI$_3$ QDs contributes to the decreased content of C-O-C bonding, owing to the decreasing value from 49 to 31.8%. Meanwhile, this value gradually decreases with the increasing RTA temperatures and shows the lowest value of 20.1% as the RTA-treated PQD film is annealed at 120 °C. As for temperatures higher than 120 °C, the values at 140 and 160 °C increase to 21.1% and then the highest, 46%. Therefore, this high temperature of 160 °C causes oxygen diffusion with a direction from the film to the annealing atmosphere, which can be visibly observed as yellow crystals. These results indicate that the appropriate annealing temperature of 120 °C can effectively reduce the binding of oxygen to carbon in PQD films, further improving crystallinity.

Table 3. The peak area for the C-C and C-O-C bonding of all samples.

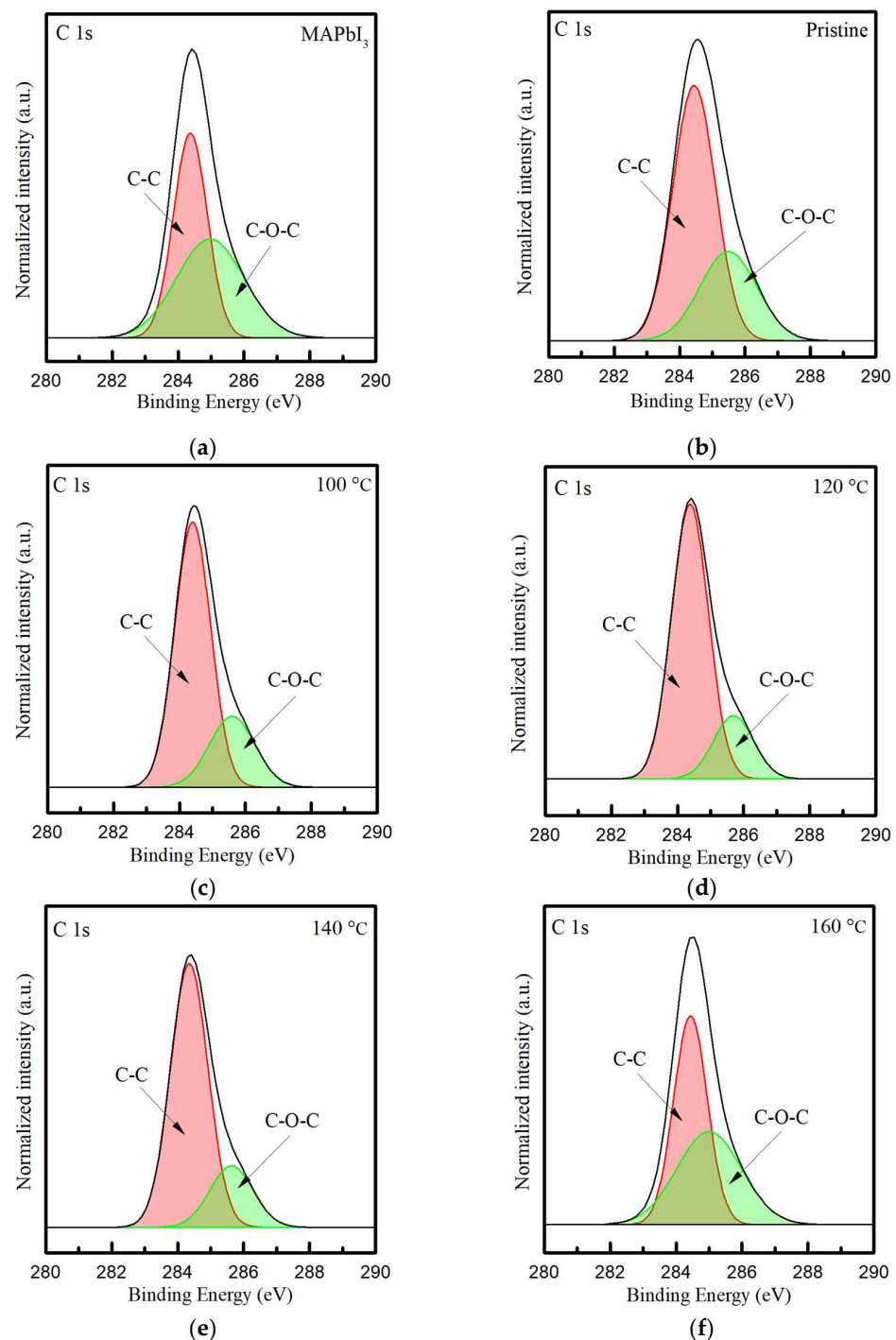| Samples ╱ Bonding (Peak Position)	MAPbI$_3$ Films	PQD Films	RTA-Treated PQD Films at Different Temperatures			
			100 °C	120 °C	140 °C	160 °C
C-C (284.4 eV)	50.9%	68.1%	74.7%	79.8%	78.8%	53.9%
C-O-C (285.4 eV)	49.0%	31.8%	25.2%	20.1%	21.1%	46.0%

Figure 5. The XPS core-level spectra of C 1s in the (**a**) MAPbI$_3$ film and (**b**) the PQD film without and with the annealing treatment at the temperatures from 100 to 160 °C (**c–f**).

To investigate the effects of the RTA temperatures on the lead (Pb) and halide substances, Figure 6a illustrates the full-wide scan of the Pb 4f core level of all samples. The characteristic binding energy values located at lower and higher levels are, respectively, assigned to Pb 4f$_{7/2}$ peak and Pb 4f$_{5/2}$ peak; in addition, the peak positions of all samples are shown in Table 4 [46]. The two peak positions of the MAPbI$_3$ film are, respectively, 138.02 and 142.91 eV [46]. Both peak positions of the PQD film, respectively, show lower binding energies of 137.8 and 142.68 eV. With the increasing RTA temperatures, at the same time, both peak positions of the PQD films continuously decrease, and then, respectively, reach the lowest value of 137.74 and 142.61 eV as the temperature reaches 140 °C. Addi-

tionally, the shift forward to a higher binding energy occurs at 160 °C. This shift forward to a lower binding energy reveals the interaction between iodine and Pb atoms to form the donor–acceptor complex, caused via cation exchange when the Pb^{2+} ion accepts a lone pair of electrons from the s orbital of $CsPbI_3$ QDs [23,48]. These results also indicate that the coordination interactions effectively suppress the existence of defects as a trap state. In addition, all samples are further deconvoluted to Pb^{2+} (137.9 and 142.8 eV) and PbO (136.3 and 141.1 eV) [49]. Correspondingly, compared to the peak area of Pb^{2+} for $MAPbI_3$ films, the values for PQD films decrease from 95.9 to 94.16%, as well as the increased peak area of Pb0 from 3.99 to 5.82%. The RTA-treated PQD films at 100–140 °C also display a lower value (2.77, 2.57, and 2.83%) of the peak area of Pb0, although the sample at 160 °C shows the highest value (10.46%) of the peak area of Pb^{2+}. This small existence of metallic Pb0 (136.3 and 141.4 eV) [50] can be attributed to the decomposition of $MAPbI_3$ films, mostly due to the chemical reaction and annealing process [51]. Furthermore, the XPS spectra of the I 3d core level of all samples are demonstrated in Figure 6b. The typical peak positions of I 3d are located at the lower $3d_{5/2}$ (618.9 and 618.7 eV) and the higher $3d_{3/2}$ (630.8 and 630.2 eV). Table 4 also reveals the peak areas of the $3d_{5/2}$ and $3d_{3/2}$ core levels of all samples. However, there is a slight peak shift of 0.08 eV when compared to the PQD films with and without the RTA process at 120 °C. This result suggests that the oxidation of Pb^{2+} is from electron donors, due to the difference in electronegativity, where the lower and higher ones are, respectively, Pb and I [52].
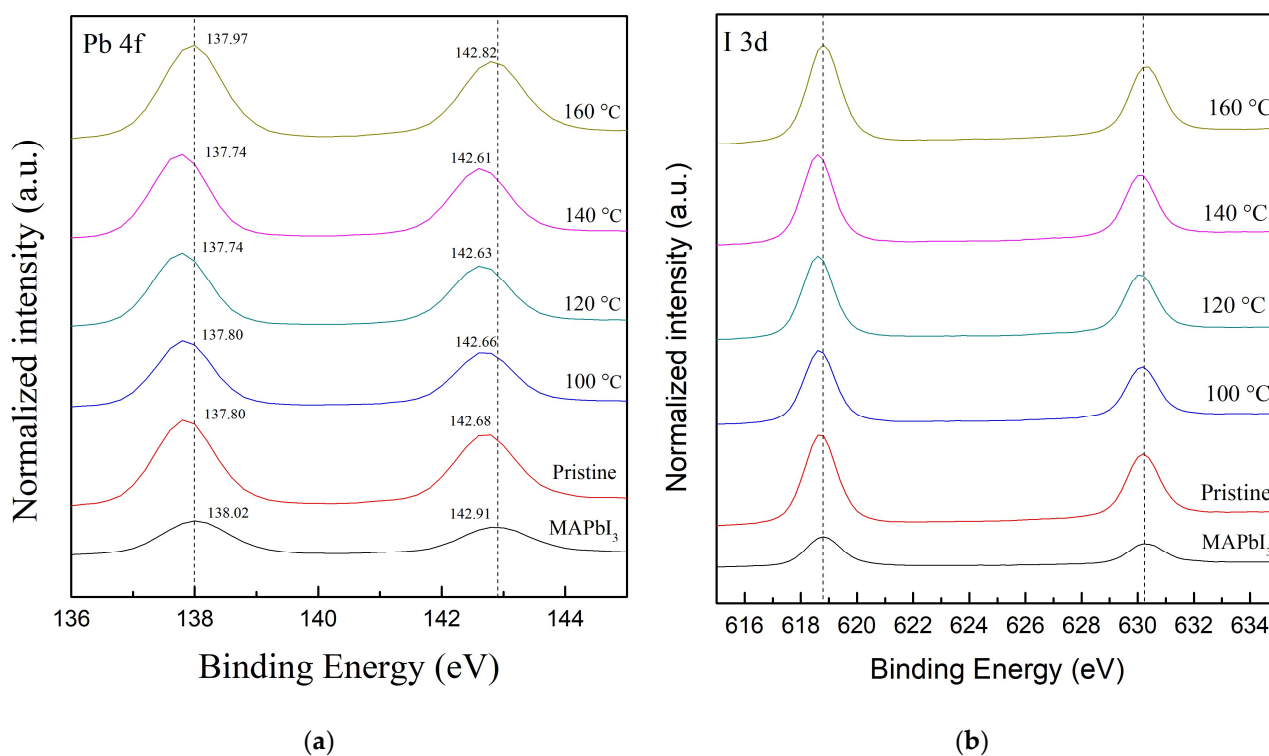

(**a**)   (**b**)

Figure 6. The XPS spectra full-wide scan of (**a**) the Pb 4f and (**b**) the I 3d core level of all samples, including the $MAPbI_3$ films and PQD films without (pristine one) and with the RTA treatment at various temperatures in the range from 100 to 160 °C. The deconvolution results are referred to in previous research [23,26].

Table 4. The peak area of both the Pb 4f ($4f_{7/2}$ and $4f_{5/2}$) and I 3d ($3d_{5/2}$ and $3d_{3/2}$) core levels of all samples.

Samples / Core-Level (Peak Position)	MAPbI$_3$ Films	PQD Films	RTA-Treated PQD Films at Different Temperatures			
			100 °C	120 °C	140 °C	160 °C
Pb $4f_{7/2}$ (138.02 eV, 137.80 eV)	55.6%/2.6%	52.8%/4.6%	55.6%/2.1%	55.4%/2.0%	54.8%/2.2%	53.2%/4.0%
Pb $4f_{5/2}$ (142.91 eV, 142.68 eV)	40.3%/1.4%	41.4%/1.2%	41.6%/0.7%	42.0%/0.6%	42.3%/0.6%	36.3%/6.5%
I $3d_{5/2}$ (618.9 eV, 618.7 eV)	22.7%/36.6%	20.0%/39.5%	18.6%/40.7%	18.3%/41.1%	20.0%/39.2%	22.5%/37.4%
I $3d_{3/2}$ (630.8 eV, 630.2 eV)	12.1%/28.4	12.6%/27.7%	13.1%/27.5%	10.9%/29.6%	11.3%/29.3%	13.0%/26.9%

4. Conclusions

This study processed perovskite-based PQD films made from MAPbI$_3$ and CsPbI$_3$ QDs using RTA in argon gas at 100–160 °C. The cation-exchanged surface structure enhances the absorbance of the samples. The RTA process effectively removes residual ligands from PQD films, raising the (110) peak intensity at 100 and 120 °C. The PQD films at 120 °C inhibit the formation of PbI$_2$ and the intermediate phase, showing a better crystallinity. As the RTA temperatures rises, oxygen and C-O-C bonding decreases to 31.4% and 20.1%, respectively. RTA contributes to residual ligands from crystallographic defects attaching to oxygen atoms, proved by the O 1s core level shifting by ~0.5 eV. At a higher temperature of 140 °C, yellow crystals are visibly observed, the films decompose, and oxygen passes from the film to the annealing environment. Meanwhile, the shift forward to a lower binding energy in the Pb 4f core level reveals the interaction between I and Pb atoms to form a donor–acceptor complex, causing the Pb^{2+} ion to accept a lone pair of electrons from the s orbital of CsPbI$_3$ QDs via cation exchange, indicating that coordination interactions effectively suppress defects as a trap state. PbI$_2$ degrades and breaks at a too-high temperature of 160 °C. Finally, compared to heating and annealing, the RTA process can effectively inhibit degradation and usefully improve PQD film performance.

Author Contributions: Conceptualization, S.-Y.L., P.-W.S., P.-H.H. and P.-J.L.; formal analysis, S.-Y.L., P.-J.L., P.-H.H. and C.-J.H.; funding acquisition, P.-J.L. and S.-Y.L.; investigation, S.-Y.L., P.-H.H. and C.-J.H.; re-sources, P.-J.L. and P.-H.H.; supervision, W.-R.C., S.-Y.L., C.-H.L. and C.-J.H.; writing—original draft, P.-J.L. and P.-H.H. All authors have read and agreed to the published version of the manuscript.

Data Availability Statement: The data presented in this study are available on request from the corresponding author.

Conflicts of Interest: The authors declare no conflict of interest.

References

1. Xie, H.; Liu, X.; Lyu, L.; Niu, D.; Wang, Q.; Huang, J.; Gao, Y. Effects of Precursor Ratios and Annealing on Electronic Structure and Surface Composition of CH$_3$NH$_3$PbI$_3$ Perovskite Films. *J. Phys. Chem. C* **2016**, *120*, 215–220. [CrossRef]
2. Kim, H.-S.; Lee, C.-R.; Im, J.-H.; Lee, K.-B.; Moehl, T.; Marchioro, A.; Moon, S.-J.; Humphry-Baker, R.; Yum, J.-H.; Moser, J.E.; et al. Lead Iodide Perovskite Sensitized All-Solid-State Submicron Thin Film Mesoscopic Solar Cell with Efficiency Exceeding 9%. *Sci. Rep.* **2012**, *2*, 591. [CrossRef] [PubMed]

3. Dunlap-Shohl, W.A.; Younts, R.; Gautam, B.; Gundogdu, K.; Mitzi, D.B. Effects of Cd Diffusion and Doping in High-Performance Perovskite Solar Cells Using CdS as Electron Transport Layer. *J. Phys. Chem. C* **2016**, *120*, 16437–16445. [CrossRef]

4. Abrusci, A.; Stranks, S.D.; Docampo, P.; Yip, H.-L.; Jen, A.K.-Y.; Snaith, H.J. High-Performance Perovskite-Polymer Hybrid Solar Cells via Electronic Coupling with Fullerene Monolayers. *Nano Lett.* **2013**, *13*, 3124–3128. [CrossRef]

5. Stranks, S.D.; Eperon, G.E.; Grancini, G.; Menelaou, C.; Alcocer, M.J.P.; Leijtens, T.; Herz, L.M.; Petrozza, A.; Snaith, H.J. Electron-Hole Diffusion Lengths Exceeding 1 Micrometer in an Organometal Trihalide Perovskite Absorber. *Science* **2013**, *342*, 341–344. [CrossRef] [PubMed]

6. Kojima, A.; Teshima, K.; Shirai, Y.; Miyasaka, T. Organometal Halide Perovskites as Visible-Light Sensitizers for Photovoltaic Cells. *J. Am. Chem. Soc.* **2009**, *131*, 6050–6051. [CrossRef]

7. Hu, J.; Liu, W.; Yang, Y.; Zhao, L.; Qiao, Y.; Li, S.; Liu, P.; Chen, M. TiO_2 Nanotube/TiO_2 Nanoparticle Hybrid Photoanode for Hole-Conductor-Free Perovskite Solar Cells Based on Carbon Counter Electrodes. *Opt. Mater. Express* **2017**, *7*, 3322. [CrossRef]

8. Li, X.; Bi, D.; Yi, C.; Décoppet, J.-D.; Luo, J.; Zakeeruddin, S.M.; Hagfeldt, A.; Grätzel, M. A Vacuum Flash–Assisted Solution Process for High-Efficiency Large-Area Perovskite Solar Cells. *Science* **2016**, *353*, 58–62. [CrossRef]

9. Yang, W.S.; Noh, J.H.; Jeon, N.J.; Kim, Y.C.; Ryu, S.; Seo, J.; Seok, S.I. High-Performance Photovoltaic Perovskite Layers Fabricated through Intramolecular Exchange. *Science* **2015**, *348*, 1234–1237. [CrossRef]

10. Wu, T.; Qin, Z.; Wang, Y.; Wu, Y.; Chen, W.; Zhang, S.; Cai, M.; Dai, S.; Zhang, J.; Liu, J.; et al. The Main Progress of Perovskite Solar Cells in 2020–2021. *Nano-Micro Lett.* **2021**, *13*, 152. [CrossRef]

11. Green, M.; Dunlop, E.; Hohl-Ebinger, J.; Yoshita, M.; Kopidakis, N.; Hao, X. Solar Cell Efficiency Tables (Version 57). *Prog. Photovolt. Res. Appl.* **2020**, *29*, 3–15. [CrossRef]

12. Green, M.A. Crystalline and Thin-Film Silicon Solar Cells: State of the Art and Future Potential. *Sol. Energy* **2003**, *74*, 181–192. [CrossRef]

13. Huang, H.; Bodnarchuk, M.I.; Kershaw, S.V.; Kovalenko, M.V.; Rogach, A.L. Lead Halide Perovskite Nanocrystals in the Research Spotlight: Stability and Defect Tolerance. *ACS Energy Lett.* **2017**, *2*, 2071–2083. [CrossRef]

14. Motti, S.G.; Meggiolaro, D.; Martani, S.; Sorrentino, R.; Barker, A.J.; De Angelis, F.; Petrozza, A. Defect Activity in Lead Halide Perovskites. *Adv. Mater.* **2019**, *31*, 1901183. [CrossRef] [PubMed]

15. Xie, F.X.; Zhang, D.; Su, H.; Ren, X.; Wong, K.S.; Grätzel, M.; Choy, W.C.H. Vacuum-Assisted Thermal Annealing of $CH_3NH_3PbI_3$ for Highly Stable and Efficient Perovskite Solar Cells. *ACS Nano* **2015**, *9*, 639–646. [CrossRef]

16. Oyewole, D.O.; Koech, R.K.; Ichwani, R.; Ahmed, R.; Hinostroza Tamayo, J.; Adeniji, S.A.; Cromwell, J.; Colin Ulloa, E.; Oyewole, O.K.; Agyei-Tuffour, B.; et al. Annealing Effects on Interdiffusion in Layered FA-Rich Perovskite Solar Cells. *AIP Adv.* **2021**, *11*, 065327. [CrossRef]

17. Li, H.; Zhou, J.; Tan, L.; Li, M.; Jiang, C.; Wang, S.; Zhao, X.; Liu, Y.; Zhang, Y.; Ye, Y.; et al. Sequential Vacuum-Evaporated Perovskite Solar Cells with More than 24% Efficiency. *Sci. Adv.* **2022**, *8*, eabo7422. [CrossRef]

18. Salado, M.; Contreras-Bernal, L.; Caliò, L.; Todinova, A.; López-Santos, C.; Ahmad, S.; Borras, A.; Idígoras, J.; Anta, J.A. Impact of Moisture on Efficiency-Determining Electronic Processes in Perovskite Solar Cells. *J. Mater. Chem. A* **2017**, *5*, 10917–10927. [CrossRef]

19. Aristidou, N.; Sanchez-Molina, I.; Chotchuangchutchaval, T.; Brown, M.; Martinez, L.; Rath, T.; Haque, S.A. The Role of Oxygen in the Degradation of Methylammonium Lead Trihalide Perovskite Photoactive Layers. *Angew. Chem. Int. Ed.* **2015**, *54*, 8208–8212. [CrossRef]

20. Aristidou, N.; Eames, C.; Sanchez-Molina, I.; Bu, X.; Kosco, J.; Islam, M.S.; Haque, S.A. Fast Oxygen Diffusion and Iodide Defects Mediate Oxygen-Induced Degradation of Perovskite Solar Cells. *Nat. Commun.* **2017**, *8*, 15218. [CrossRef]

21. Zhang, L.; Sit, P.H.-L. Ab Initio Study of the Role of Oxygen and Excess Electrons in the Degradation of $CH_3NH_3PbI_3$. *J. Mater. Chem. A* **2017**, *5*, 9042–9049. [CrossRef]

22. Philippe, B.; Park, B.-W.; Lindblad, R.; Oscarsson, J.; Ahmadi, S.; Johansson, E.M.J.; Rensmo, H. Chemical and Electronic Structure Characterization of Lead Halide Perovskites and Stability Behavior under Different Exposures—A Photoelectron Spectroscopy Investigation. *Chem. Mater.* **2015**, *27*, 1720–1731. [CrossRef]

23. Lien, S.-Y.; Chen, Y.-H.; Chen, W.-R.; Liu, C.-H.; Huang, C.-J. Effect of Growth Temperature on the Characteristics of CsPbI3-Quantum Dots Doped Perovskite Film. *Molecules* **2021**, *26*, 4439. [CrossRef] [PubMed]

24. Martin, C.; Prudnikau, A.; Orazi, L.; Gaponik, N.; Lesnyak, V. Selectively Tunable Luminescence of Perovskite Nanocrystals Embedded in Polymer Matrix Allows Direct Laser Patterning. *Adv. Opt. Mater.* **2022**, *10*, 2200201. [CrossRef]

25. Huang, P.-H.; Chen, Y.-H.; Lien, S.-Y.; Lee, K.-W.; Wang, N.-F.; Huang, C.-J. Effect of Annealing on Innovative CsPbI3-QDs Doped Perovskite Thin Films. *Crystals* **2021**, *11*, 101. [CrossRef]

26. Lien, S.-Y.; Lai, P.-J.; Chen, W.-R.; Liu, C.-H.; Sze, P.-W.; Huang, C.-J. The Annealing Effect at Different Temperatures for Organic-Inorganic Perovskite Quantum Dots. *Crystals* **2022**, *12*, 204. [CrossRef]

27. Dou, B.; Pool, V.L.; Toney, M.F.; van Hest, M.F.A.M. Radiative Thermal Annealing/in Situ X-Ray Diffraction Study of Methylammonium Lead Triiodide: Effect of Antisolvent, Humidity, Annealing Temperature Profile, and Film Substrates. *Chem. Mater.* **2017**, *29*, 5931–5941. [CrossRef]

28. Wright, N.E.; Qin, X.; Xu, J.; Kelly, L.L.; Harvey, S.P.; Toney, M.F.; Blum, V.; Stiff-Roberts, A.D. Influence of Annealing and Composition on the Crystal Structure of Mixed-Halide, Ruddlesden–Popper Perovskites. *Chem. Mater.* **2022**, *34*, 3109–3122. [CrossRef]

29. Senger, C.; Fan, X.; Pagaduan, J.N.; Zhang, X.; Ping, J.; Katsumata, R. Defect Healing in Graphene via Rapid Thermal Annealing with Polymeric "Nanobandage.". *Small* **2022**, 2206295. [CrossRef]

30. Xu, L.; Yuan, S.; Zeng, H.; Song, J. A Comprehensive Review of Doping in Perovskite Nanocrystals/Quantum Dots: Evolution of Structure, Electronics, Optics, and Light-Emitting Diodes. *Mater. Today Nano* **2019**, *6*, 100036. [CrossRef]

31. Niu, G.; Li, W.; Li, J.; Liang, X.; Wang, L. Enhancement of Thermal Stability for Perovskite Solar Cells through Cesium Doping. *RSC Adv.* **2017**, *7*, 17473–17479. [CrossRef]

32. Han, J.; Luo, S.; Yin, X.; Zhou, Y.; Nan, H.; Li, J.; Li, X.; Oron, D.; Shen, H.; Lin, H. Hybrid PbS Quantum-Dot-in-Perovskite for High-Efficiency Perovskite Solar Cell. *Small* **2018**, *14*, 1801016. [CrossRef]

33. Jancik Prochazkova, A.; Scharber, M.C.; Yumusak, C.; Jančík, J.; Másilko, J.; Brüggemann, O.; Weiter, M.; Sariciftci, N.S.; Krajcovic, J.; Salinas, Y.; et al. Synthesis Conditions Influencing Formation of MAPbBr$_3$ Perovskite Nanoparticles Prepared by the Ligand-Assisted Precipitation Method. *Sci. Rep.* **2020**, *10*, 15720. [CrossRef]

34. Zhang, Y.; Yang, Y.; Zhang, X.; Wang, T.; Nian, L.; Rong, Q.; Zhou, G.; Li, N. Low Temperature Preparation of All-Inorganic CsPbI$_3$ Perovskite Solar Cells with Ethanediamine as Additive. *Org. Electron.* **2020**, *87*, 105940. [CrossRef]

35. Shu, B.; Chang, Y.; Zhang, J.; Cheng, X.; Yu, D. Synthesis and Photoluminescence Kinetics of Ce^{3+}-Doped CsPbI$_3$ QDs with near-Unity PLQY. *Nano Res.* **2021**, *14*, 3352–3357. [CrossRef]

36. Smith, A.M.; Mohs, A.M.; Nie, S. Tuning the Optical and Electronic Properties of Colloidal Nanocrystals by Lattice Strain. *Nat. Nanotechnol.* **2009**, *4*, 56–63. [CrossRef]

37. Luo, S.; Kazes, M.; Lin, H.; Oron, D. Strain-Induced Type II Band Alignment Control in CdSe Nanoplatelet/ZnS-Sensitized Solar Cells. *J. Phys. Chem. C* **2017**, *121*, 11136–11143. [CrossRef]

38. Senocrate, A.; Acartürk, T.; Kim, G.Y.; Merkle, R.; Starke, U.; Grätzel, M.; Maier, J. Interaction of Oxygen with Halide Perovskites. *J. Mater. Chem. A* **2018**, *6*, 10847–10855. [CrossRef]

39. Guo, X.; McCleese, C.; Kolodziej, C.; Samia, A.C.S.; Zhao, Y.; Burda, C. Identification and Characterization of the Intermediate Phase in Hybrid Organic–Inorganic MAPbI$_3$ Perovskite. *Dalton Trans.* **2016**, *45*, 3806–3813. [CrossRef]

40. Damle, V.H.; Gouda, L.; Tirosh, S.; Tischler, Y.R. Structural Characterization and Room Temperature Low-Frequency Raman Scattering from MAPbI$_3$ Halide Perovskite Films Rigidized by Cesium Incorporation. *ACS Appl. Energy Mater.* **2018**, *1*, 6707–6713. [CrossRef]

41. Bouich, A.; Marí-Guaita, J.; Bouich, A.; Pradas, I.G.; Marí, B. Towards Manufacture Stable Lead Perovskite APbI$_3$ (A = Cs, MA, FA) Based Solar Cells with Low-Cost Techniques. In Proceedings of the 1st International Conference on Energy, Power and Environment, Gujrat, Pakistan, 11–12 November 2021; p. 81.

42. Da Silva Filho, J.M.C.; Landers, R.; Marques, F.C. Lead Iodide and Perovskite Films Obtained by Iodination of PbS Thin Films. *J. Inorg. Organomet. Polym.* **2019**, *29*, 2161–2167. [CrossRef]

43. Mishra, A.; Ahmad, Z.; Touati, F.; Shakoor, R.A.; Nazeeruddin, M.K. One-Dimensional Facile Growth of MAPbI$_3$ Perovskite Micro-Rods. *RSC Adv.* **2019**, *9*, 11589–11594. [CrossRef] [PubMed]

44. Collins, G.; Davitt, F.; O'Dwyer, C.; Holmes, J.D. Comparing Thermal and Chemical Removal of Nanoparticle Stabilizing Ligands: Effect on Catalytic Activity and Stability. *ACS Appl. Nano Mater.* **2018**, *1*, 7129–7138. [CrossRef]

45. Rocks, C.; Svrcek, V.; Maguire, P.; Mariotti, D. Understanding Surface Chemistry during MAPbI$_3$ Spray Deposition and Its Effect on Photovoltaic Performance. *J. Mater. Chem. C* **2017**, *5*, 902–916. [CrossRef]

46. Ahmad, Z.; Najeeb, M.A.; Shakoor, R.A.; Alashraf, A.; Al-Muhtaseb, S.A.; Soliman, A.; Nazeeruddin, M.K. Instability in CH$_3$NH$_3$PbI$_3$ Perovskite Solar Cells Due to Elemental Migration and Chemical Composition Changes. *Sci. Rep.* **2017**, *7*, 15406. [CrossRef] [PubMed]

47. Li, J.; Zeng, X.; Ren, T.; van der Heide, E. The Preparation of Graphene Oxide and Its Derivatives and Their Application in Bio-Tribological Systems. *Lubricants* **2014**, *2*, 137–161. [CrossRef]

48. Li, B.; Zhen, J.; Wan, Y.; Lei, X.; Liu, Q.; Liu, Y.; Jia, L.; Wu, X.; Zeng, H.; Zhang, W.; et al. Anchoring Fullerene onto Perovskite Film via Grafting Pyridine toward Enhanced Electron Transport in High-Efficiency Solar Cells. *ACS Appl. Mater. Interfaces* **2018**, *10*, 32471–32482. [CrossRef]

49. Chu, L.; Hu, R.; Liu, W.; Ma, Y.; Zhang, R.; Yang, J.; Li, X. Screen Printing Large-Area Organometal Halide Perovskite Thin Films for Efficient Photodetectors. *Mater. Res. Bull.* **2018**, *98*, 322–327. [CrossRef]

50. Zhao, L.; Kerner, R.A.; Xiao, Z.; Lin, Y.L.; Lee, K.M.; Schwartz, J.; Rand, B.P. Redox Chemistry Dominates the Degradation and Decomposition of Metal Halide Perovskite Optoelectronic Devices. *ACS Energy Lett.* **2016**, *1*, 595–602. [CrossRef]

51. Lindblad, R.; Bi, D.; Park, B.; Oscarsson, J.; Gorgoi, M.; Siegbahn, H.; Odelius, M.; Johansson, E.M.J.; Rensmo, H. Electronic Structure of TiO$_2$/CH$_3$NH$_3$PbI$_3$ Perovskite Solar Cell Interfaces. *J. Phys. Chem. Lett.* **2014**, *5*, 648–653. [CrossRef]

52. Li, X.; Wu, S.; Chen, Y.; Tang, J.; Liu, M.; Chen, Z.; Zhang, P.; Li, S. Grain Boundary Defect Controlling of Perovskite via *N*-Hydroxysuccinimide Post-Treatment Process in Efficient and Stable n–i–p Perovskite Solar Cells. *Sol. RRL* **2022**, *6*, 2200502. [CrossRef]